

Article

Corrosion Behavior of Pipeline Carbon Steel under Different Iron Oxide Deposits in the District Heating System

Yong-Sang Kim and Jung-Gu Kim *

School of Advanced Materials Engineering, Sungkyunkwan University, 300 Chunchun-Dong, Jangan-Gu, Suwon 440-746, Korea; skybyego@gmail.com

* Correspondence: kimjg@skku.edu; Tel.: +82-31-2907360

Academic Editor: Laichang Zhang

Received: 21 April 2017; Accepted: 17 May 2017; Published: 19 May 2017

Abstract: The corrosion behavior of pipeline steel covered by iron oxides (α -FeOOH; Fe_3O_4 and Fe_2O_3) was investigated in simulated district heating water. In potentiodynamic polarization tests; the corrosion rate of pipeline steel is increased under the iron oxide but the increasing rate is different due to the different chemical reactions of the covered iron oxides. Pitting corrosion was only observed on the α -FeOOH-covered specimen; which is caused by the crevice corrosion under the α -FeOOH. From Mott-Schottky and X-ray diffraction results; the surface reaction and oxide layer were dependent on the kind of iron oxides. The iron oxides deposit increases the failure risk of the pipeline and localized corrosion can be occurred under the α -FeOOH-covered region of the pipeline. Thus, prevention methods for the iron oxide deposit in the district pipeline system such as filtering or periodic chemical cleaning are needed.

Keywords: corrosion; polarization; iron oxide; Mott-Schottky; carbon steel

1. Introduction

A district heating (DH) system provides heat for inhabitants of large cities in an economical manner. Heat from heat and power generating plants and large heat sources is cheaper than heat produced in individual, low-power boiler rooms [1]. There are many merits to DH systems, including increased energy efficiencies, reduced life cycle costs, and elevated control over environmental impacts [2,3]. Additionally, the high efficiencies of DH systems decrease the emission of combustion products into the atmosphere. Because of these advantages, many countries such as Denmark, Russia, Finland, and Canada are developing DH systems, and the market share is reported to be approximately 50% [4,5]. Additionally, a DH system was introduced to Korea in 1987 and applied to various fields.

A DH system becomes more useful with more satellite and planned cities near each megalopolis. A DH system has a long stagnation period due to the construction of numerous urban housing facilities and infrastructure. Additionally, maintenance and improvement work are ongoing. During this period, the pipeline in the distribution part of the DH system is exposed to low temperature ($\sim 40^\circ\text{C}$) water with little or no flow. The long stagnation condition has problems associated with corrosion such as deposits from solid particles (sand, debris, and iron oxides), ion conductivity, ferrous ions, and dissolved oxygen [6–9]. The deposits on the internal surface of a pipeline especially cause serious localized corrosion (such as pitting corrosion and crevice corrosion), which is identified as under deposit corrosion (UDC) [10–12].

UDC is unlike other corrosion forms, as the conditions, such as pH and concentration of the aggressive species, under the deposit are different from the conditions in regions without deposits. As a result, there will be galvanic corrosion between the areas under the deposit and the areas without

deposit [13–17]. Because of these properties, UDC is a serious problem in pipeline systems due to the potential for unexpected failure from localized damage. In order to prevent pipeline failure from UDC, it is important to investigate the mechanism of UDC. Jeannin et al. determined that the corrosion process of carbon steel differed according to the type of deposited minerals (silica, kaolinite, chlorite, and montmorillonite) [11]. Zhang et al. identified galvanic corrosion between the covered mixed deposit on the carbon steel and bare carbon steel (uncovered mixed deposit) in a gas filled environment [17]. However, the deposit is composed of not only minerals (clay and sand) but also corrosion products (iron oxide and carbonate etc.); this is because the corrosion products float in fluid, combine with each other, and are deposited under stagnant conditions. Therefore, the corrosion process under different corrosion product deposits is an important study.

The corrosion products can inhibit further corrosion by shielding the metal from the environment. However, there are cases where corrosion products accelerate corrosion [18]. The corrosion process can be dependent on the oxide film because the oxide is directly formed in close connection with the crystal of the metal while the deposit is stacked on the metal [19]. In this work, the corrosion behavior of carbon steel under different iron oxides, such as α -FeOOH (goethite), Fe_3O_4 (magnetite), and Fe_2O_3 (hematite) was evaluated by electrochemical measurements and surface characterization. These iron oxides are usually produced on the pipeline surface in the DH system. The formation of these oxides depends on the presence of the oxygen in the water. The Fe_3O_4 is generally formed in the de-aerated district water but α -FeOOH and Fe_2O_3 are generated in the aeration condition. Also, the damaged surface, which is mesas formed by corrosion, has been observed under the iron oxide. Thus, in this study, the influence of each oxide on the corrosion behavior is investigated for clear understanding of the UDC by iron oxides in the district heating system. Furthermore, the corrosion mechanism under different iron oxides was investigated to prevent unexpected corrosion and failure in the DH system from UDC.

2. Materials and Methods

2.1. Materials and Solution Preparation

The material used in this work was a pipeline carbon steel which is the standard material in the American society of testing and materials (ASTM A135). Table 1 lists the steel composition. Specimens were machined into 1 cm² square shapes and sealed with epoxy resin. Before the deposition process, the specimens were abraded with silicon carbide paper starting from 100- to 600-grit size, and then rinsed with deionized water and cleaned with ethanol.

Table 1. Chemical composition of tested pipeline steel (wt %).

C	Si	Mn	P	S	Fe
0.25	0.35	0.50	0.040	0.040	Balance

Table 2 lists the chemical composition of the simulated district heating water, which is based on actual district heating water over 10 years as measured in its stagnant condition. To adjust the chemical composition of the test solution, the pH was adjusted with a 0.1 M NaOH solution. Although the heating water was usually soft and pure, the detection of ferric ions (Fe^{3+}) and chloride ions (Cl^-) is attributed to the long stagnation condition [6]. Prior to testing, the solution was de-aerated by purging with N_2 (99.999%) for 2 h because the DH system is blocked from the outside, i.e., it is a closed system so that the amount of dissolved oxygen is very low. The temperature is maintained at 40 °C using a constant-temperature water bath.

Table 2. Chemical composition of the simulated district heating water (mg/L).

pH	FeCl_3	NaNO_2	NaNO_3	NaCl
9.8	16.25	7.5	0.7	65.2

2.2. Deposition Process

The three iron oxides (α -FeOOH, Fe_3O_4 and Fe_2O_3) used in this study were purchased from SAMCHUN chemical corporation (Pyeongtaek-si, Korea). The powder X-ray diffraction analysis is shown in Figure 1 and the iron oxides were confirmed with the diffraction database. Because the powder-state iron oxides are difficult to deposit on the specimen, ethanol was mixed with the iron oxides. The specimen was covered with a rubber 'O' shaped ring (diameter: 3 cm, height: 3 mm) and then filled with iron oxide mixed with ethanol, which has the same thickness as the rubber ring, approximately 3 mm, to simulate the UDC environment. Before immersion in the test solution for the electrochemical tests, the deposit-covered specimen was dried in air for 30 minutes to vaporize the ethanol.

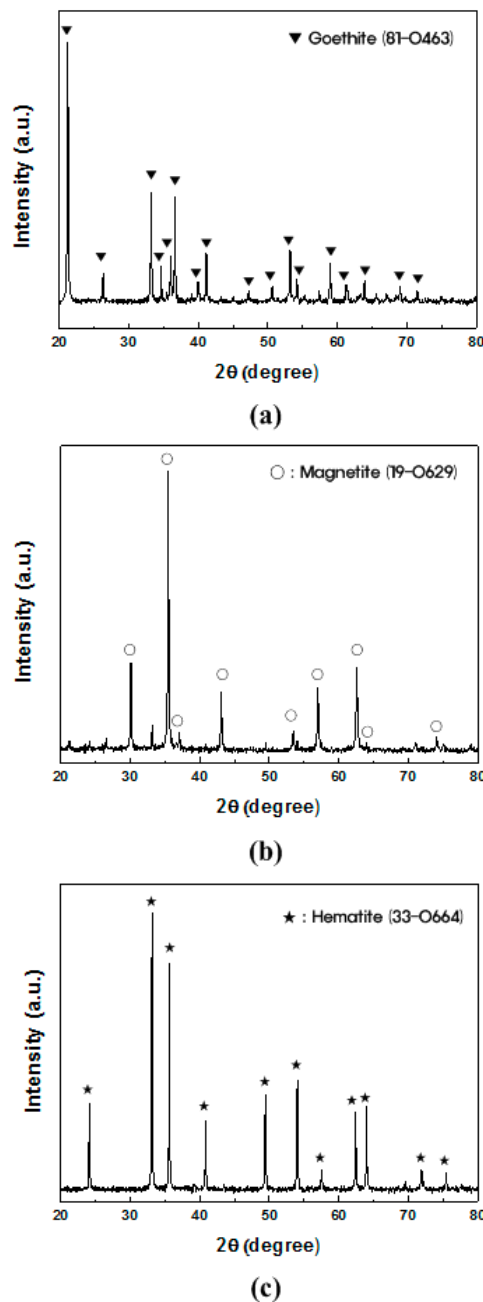


Figure 1. X-ray diffraction results of iron oxide powder used as deposit materials: (a) α -FeOOH; (b) Fe_3O_4 ; (c) Fe_2O_3 .

2.3. Electrochemical Measurements

Electrochemical tests were conducted to evaluate the corrosion behavior and properties of the iron oxide deposits. A three-electrode electrochemical cell was constructed with the SPPS 38 carbon steel electrode, uncovered and covered with iron oxide deposits as the working electrode (WE), two pure graphite rods as the counter electrodes (CE), and a saturated calomel electrode (SCE) as the reference electrode (RE). In potentiodynamic polarization tests, the specimens were fully covered with iron oxide deposits (1 cm²), and a stainless steel rod covered with glass for preventing contact with the solution was used for the electric connection with the WE. The dynamic voltage (IR) drop was automatically compensated in the potentiostat because the simulated district heating water has low conductivity (347 μS/cm). The schematic of the three-electrode electrochemical cell used in this experiment is shown in Figure 2. Before potentiodynamic polarization tests, the working electrode was immersed in the test solution for 6 h until a steady state was reached, and the open-circuit potential (OCP) was obtained. Potentiodynamic polarization curves were measured by scanning the potential from −250 mV versus OCP to 400 mV_{SCE} at a sweep rate of 0.166 mV/s. The electrochemical impedance spectroscopy (EIS) was performed at the OCP with amplitude of 10 mV at frequencies ranging from 10,000 to 0.01 Hz.

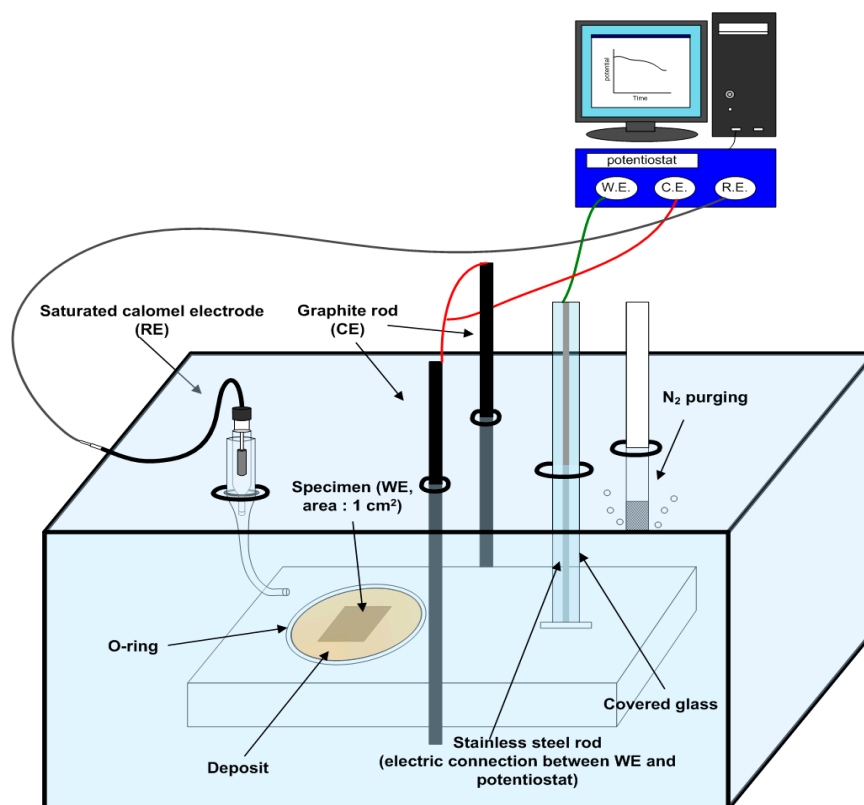


Figure 2. Schematic of three-electrode electrochemical cell used in this study.

To accelerate the corrosion process, potentiostatic tests were performed at an applied potential of -0.65 mV_{SCE}, slightly greater than the corrosion potential (E_{corr}) of each specimen for 20 h. The fully deposit-covered specimens were evaluated to observe the corrosion process under the deposits. Additionally, to investigate the difference in corrosion behavior for covered and uncovered deposits, the deposit was designed to cover only half of the specimen. After potentiostatic tests, the iron oxide deposits and corrosion products on the carbon steel surface were removed and cleaned for 10 min in the cleaning solution containing 500 mL HCl (37% concentration), 3.5 g hexamethylenetetramine (C₆H₁₂N₄), and distilled water to produce 1000 mL. The specimens were then rinsed in distilled water and dried with nitrogen gas.

To analyze the surface properties of uncovered and covered deposit specimens, Mott-Schottky measurements were performed with a PARSTAT 2263 (Princeton Applied Research, Oak Ridge, TN, USA). Before the Mott-Schottky measurements, each specimen was immersed in the test solution for 340 h. The Mott-Schottky plots were obtained by sweeping in the positive direction at a frequency of 1 kHz with an amplitude signal of 10 mV, a potential range of $-0.7 V_{SCE}$ to $0.1 V_{SCE}$, and a potential step of 25 mV. All electrochemical tests were performed three times to ensure reproducibility.

2.4. Surface Characterization

After the potentiostatic tests, the morphology (surface and cross-section) of the corroded specimens was observed using optical microscopy (OM). The specimen after potentiostatic test was cut by micro cutting machine, and then produced epoxy mounting. To clear observation of the damaged surface, the surface was cleaned by cleaning solution containing 500 mL HCl, 3.5 g hexamethylenetetramine ($C_6H_{12}N_4$) and distilled water to make 1000 mL for 10 min. Additionally, to investigate the surface condition under the oxide deposits, the specimens were analyzed by X-ray diffraction (XRD, D8 Advanced, Bruker, Billerica, MA, USA) using Cu-K α radiation operated at 18 kW with a scanning speed of $2^\circ / \text{min}$ after 340 h of immersion. Before the XRD analysis, the deposit on the specimens was removed by distilled water and dried with N_2 gas to prevent additional oxidation. The XRD patterns were analyzed by the diffraction database.

3. Results

3.1. Potentiodynamic Polarization Tests

Figure 3 shows the polarization curves in the form of $I = f(E)$ and with the extrapolated Tafel slopes of a bare specimen and different iron oxides ($\alpha\text{-FeOOH}$, Fe_3O_4 , Fe_2O_3)-covered specimens after a 6 h immersion in the test solution at 40°C . All of the polarization curves showed active corrosion behavior. In the Fe_3O_4 and $\alpha\text{-FeOOH}$ cases, the current densities of cathodic and anodic polarization curves were increased compared to the bare specimen, and the corrosion potentials were negatively shifted. This indicates that the Fe_3O_4 and $\alpha\text{-FeOOH}$ deposits increased the cathodic and anodic reactions on the surface. Alternatively, in the case of Fe_2O_3 , only the cathodic current density increased and the corrosion potential was not shifted.

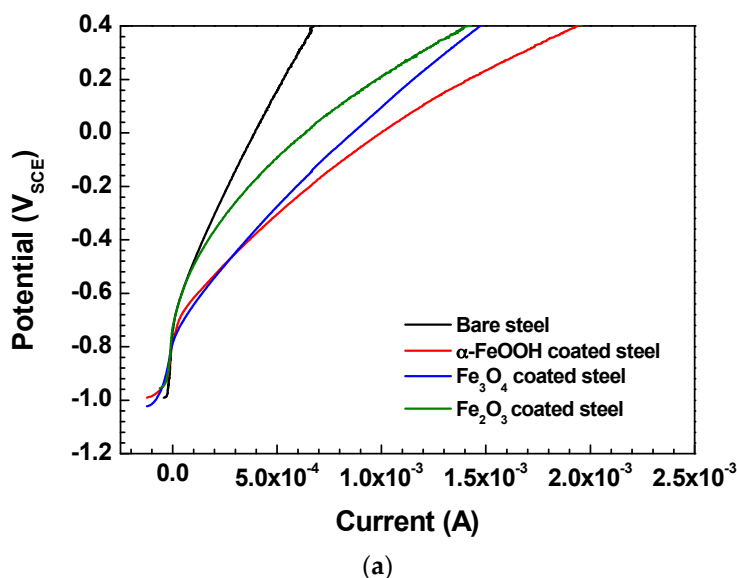


Figure 3. Cont.

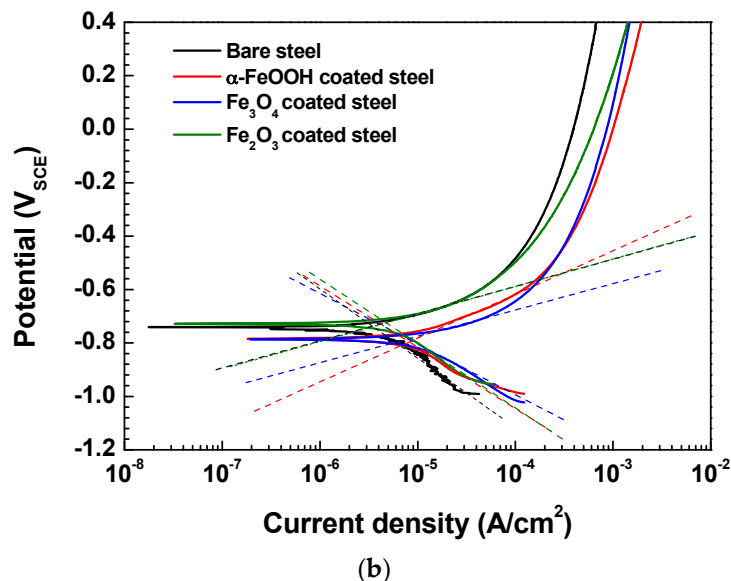


Figure 3. (a) Polarization curves in the form of $I = f(E)$ and (b) polarization curves with Tafel slopes of the specimens covered with different iron oxides (α -FeOOH, Fe_3O_4 , Fe_2O_3) and uncovered after 6 h of immersion in the simulated district heating water at 40 °C.

The corresponding kinetic parameters in the polarization curves, such as the corrosion potential (E_{corr}), corrosion current density (i_{corr}), polarization resistance (R_p), and anodic and cathodic Tafel slopes (β_a , β_c), are listed in Table 3. The i_{corr} and E_{corr} values were different for the iron oxide-covered specimens, and i_{corr} was related to the corrosion rate according to Faraday's law:

$$\text{Corrosionrate (mm/yr)} = \frac{3.16 \times 10^8 \times i_{corr} \times M}{z \times F \times \rho} \quad (1)$$

where M is the molar mass of the metal (g/mol), z is the number of electrons transferred per metal atom, F is the Faraday's constant, and ρ is the density of the metal (g/cm³). Thus, i_{corr} was increased in all oxide-covered specimens, indicating the deposit state of the iron oxides increased the corrosion of the steel substrate. Also, the polarization resistance was calculated by the following equation [20]:

$$R_p = \frac{\beta_a \times \beta_c}{2.3 \times i_{corr} \times (\beta_a + \beta_c)} \quad (2)$$

Table 3. Electrochemical parameters of the polarization curves of the bare specimen and iron oxides (α -FeOOH, Fe_3O_4 , Fe_2O_3)-covered specimens in the simulated district heating water at 40 °C.

Specimen	β_a (mV/Decade)	β_c (mV/Decade)	E_{corr} (mV _{SCE})	i_{corr} ($\mu\text{A}/\text{cm}^2$)	R_p ($\Omega \cdot \text{cm}^2$)	Corrosion Rate (mm/Year)
Bare	102 ± 3	−246 ± 12	−741 ± 5	3.876 ± 0.05	8088	0.045
α -FeOOH	122 ± 6	−215 ± 5	−775 ± 6	9.123 ± 0.03	3323	0.106
Fe_3O_4	99 ± 12	−202 ± 9	−786 ± 21	8.692 ± 0.1	3709	0.101
Fe_2O_3	105 ± 5	−265 ± 15	−735 ± 11	5.311 ± 0.09	6156	0.061

The i_{corr} and R_p are related to the corrosion resistance of the materials, and these were increased or decreased by the covered iron oxide, respectively. Consequently, it means that the corrosion reactions were affected by Fe_3O_4 and α -FeOOH deposits and the three iron oxide deposits (α -FeOOH, Fe_3O_4 and Fe_2O_3) affected the cathodic reactions [21–23]. The β_a and β_c were changed according to the kind

of covered iron oxides. In the case of α -FeOOH, the β_a was increased while the β_c was decreased in comparison with the bare specimen. It indicates that the α -FeOOH influenced the anodic and cathodic reactions on the steel surface. On the other hand, the β_a was not significantly changed and β_c was changed in the cases of Fe_3O_4 and Fe_2O_3 , meaning that the Fe_3O_4 and Fe_2O_3 , mainly had an effect on the cathodic reaction than anodic reaction.

3.2. Electrochemical Impedance Spectroscopy (EIS)

Figure 4 presents the EIS results in the form of the Bode phase and impedance plots for specimens covered with different iron oxides (α -FeOOH, Fe_3O_4 , and Fe_2O_3) and uncovered after 6 h immersion in the simulated district heating water at 40 °C. The Bode plot produces a more detailed explanation of the electrochemical frequency-dependent property than the Nyquist plot [24]. The high frequency spectra indicated local surface defect, whereas the low frequency spectra indicated the process within the film and at the metal/film interface [25]. The absolute impedance value of the specimen covered by iron oxides is less than that of the bare specimen. The absolute impedance value decreases in the following order: α -FeOOH > Fe_3O_4 > Fe_2O_3 > bare, which is the same trend as the corrosion current density in the potentiodynamic polarization tests. Additionally, the phase angle maximum decreased in the same order: α -FeOOH > Fe_3O_4 > Fe_2O_3 > bare, and the shoulder on the phase angle curve of the bare pipe shifted to a lower frequency. The results were due to inhomogeneity or porosity in the surface film [26], indicating that the surface film deteriorates after being covered with iron oxides, especially in the case of the α -FeOOH-covered specimen.

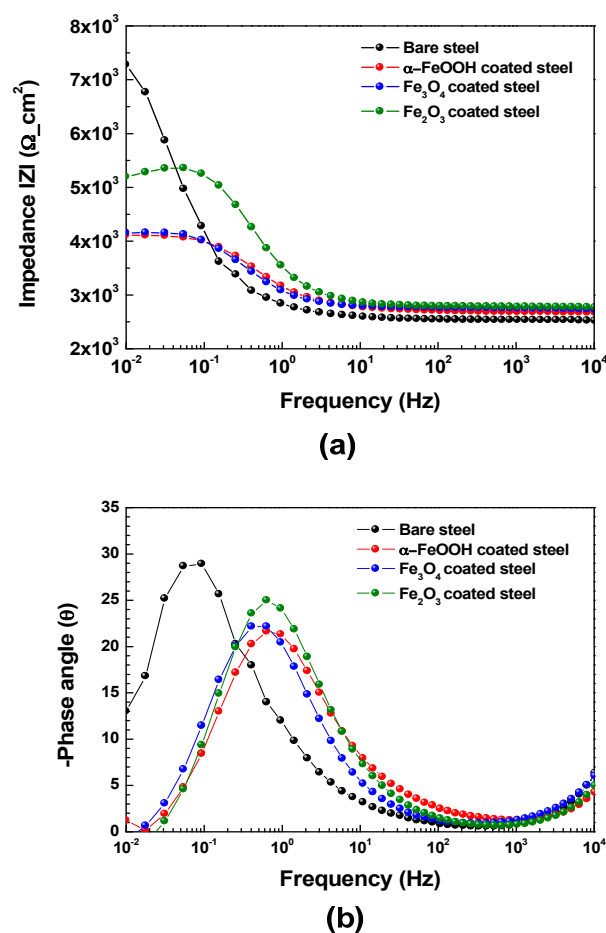


Figure 4. Bode plots of (a) impedance and (b) phase angle vs. frequency for specimens covered with different iron oxides (α -FeOOH, Fe_3O_4 , Fe_2O_3) and uncovered after 6 h of immersion in the simulated district heating water at 40 °C.

Figure 5 shows the equivalent circuit to fit the results of the EIS tests. In this equivalent circuit, the R_s is the solution resistance, CPE1 (CPE: constant phase element) is the dielectric property of the film and water absorbed on the film, R_{film} is the electrical resistance resulting from the ionic path of the pores in the film, CPE2 is the capacitance generated by metal dissolution and the electric double layer, and R_{ct} is the resistance associated with metal dissolution. The CPE is applied in this equivalent circuit instead of a perfect capacitor to produce a more accurate fit and interpretation [27,28]. The impedance of CPE is expressed as:

$$Z_{CPE} = \frac{1}{Y_0(j\omega)^n} \quad (3)$$

where Y_0 is the magnitude of CPE, j is the imaginary unit ($j^2 = -1$), α is the phase angle of CPE, and $n = \alpha/(\pi/2)$. The parameter n typically lies between 0.50 and 1.0, and CPE expresses an ideal capacitor at $n = 1$. The parameter n is often referred to as the frequency dispersion due to surface states like inhomogeneity [29,30] and roughness [31].

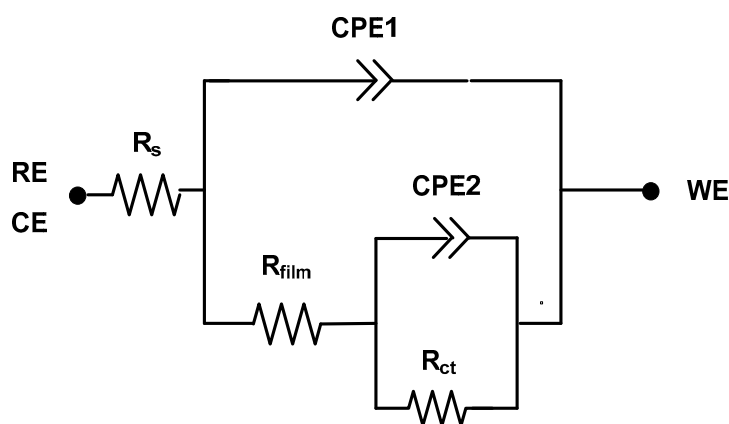


Figure 5. Equivalent circuit to fit the electrochemical impedance spectroscopy (EIS) data.

Some parameters extracted from the EIS data are listed in Table 4. To calculate the double layer capacitance (C_{dl}), the following equation was used:

$$C_{dl} = Y_0(2\pi f_{max})^{n-1} \quad (4)$$

In Equation (4), C_{dl} is the double layer capacitance and f_{max} is the frequency at which the imaginary component of the impedance reaches the maximum value. The ZSimpwin program (v3.2, Princeton Applied Research, Oak Ridge, TN, USA) was used to fit the EIS data, which is presented in Table 4. Figure 6 shows the R_{film} and R_{ct} of the specimens. R_{film} and R_{ct} decreased for the iron oxide-covered specimens in the following order: α -FeOOH > Fe_3O_4 > Fe_2O_3 > bare. The covered iron oxides had the lower corrosion resistance than bare specimen. Additionally, the n value in the case of α -FeOOH was the lowest, indicating an unstable surface film due to pores and defects on the surface.

Table 4. Impedance parameters of bare specimen and iron oxides (α -FeOOH, Fe_3O_4 and Fe_2O_3)-covered specimens in the simulated district heating water at 40 °C.

Specimen	R_s ($\Omega \cdot \text{cm}^2$)	R_{film} ($\Omega \cdot \text{cm}^2$)	n	C_{film} ($\mu\text{F} \cdot \text{s}^{n-1} / \text{cm}^2$)	R_{ct} ($\Omega \cdot \text{cm}^2$)	n	C_{dl} ($\mu\text{F} \cdot \text{s}^{n-1} / \text{cm}^2$)
Bare	2653 ± 158	1427 ± 52	0.98 ± 0.01	53 ± 5	6237 ± 236	0.88 ± 0.01	582.2 ± 22
α -FeOOH	2712 ± 72	648 ± 23	0.72 ± 0.05	19 ± 3	1485 ± 118	0.83 ± 0.01	621.8 ± 8
Fe_3O_4	2759 ± 123	709 ± 11	0.78 ± 0.02	220 ± 6	1582 ± 85	0.83 ± 0.02	889.6 ± 56
Fe_2O_3	2788 ± 201	1071 ± 105	0.84 ± 0.01	151 ± 11	2730 ± 351	0.86 ± 0.02	782.5 ± 78

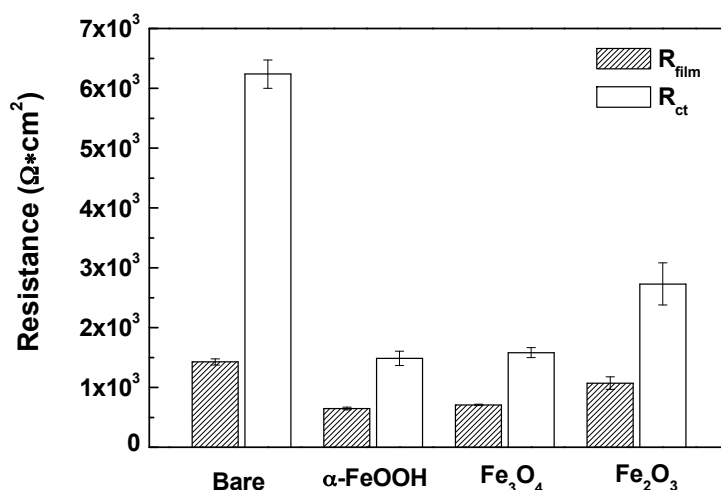


Figure 6. R_{film} and R_{ct} of the specimens covered with different iron oxides (α -FeOOH, Fe₃O₄, Fe₂O₃) and uncovered after 6 h immersion in the simulated district heating water at 40 °C.

3.3. Potentiostatic Tests

Potentiostatic tests were conducted to investigate the corrosion behavior of the iron oxide-covered specimens. Additionally, to identify galvanic corrosion between covered and uncovered specimens, half of the specimen was covered with deposit. Figure 7 shows the specimen covered iron oxides after potentiostatic tests under $-650 \text{ mV}_{\text{SCE}}$ for 20 h in the test solution at 40 °C. As shown in Figure 7a, significant pitting was observed on the α -FeOOH-covered specimen and the size of the pits ranged from 150 to 300 μm . However, as shown in Figure 7b,c, pitting was not observed on the Fe₃O₄ and Fe₂O₃-covered specimens. Figure 8 shows the cross section of the α -FeOOH-covered specimen after the potentiostatic test. As shown in Figure 8, pitting was observed on the α -FeOOH-covered specimen and the depth of the pitting was approximately 170 μm . This indicates that the corrosion behavior was different in the α -FeOOH, Fe₃O₄, and Fe₂O₃ cases.

Figure 9 shows the boundary of the specimens with covered (left side) and uncovered (right side) deposits after potentiostatic tests under $-650 \text{ mV}_{\text{SCE}}$ for 20 h at 40 °C. In Figure 9a,b, the corrosion was accelerated at the boundary of the α -FeOOH and Fe₃O₄-covered specimens, which was caused by more negative corrosion potential than the bare specimen, i.e., a galvanic effect. Alternatively, the boundary between the Fe₂O₃-covered and uncovered did not show accelerating corrosion behavior as shown in Figure 9c, which could be due to the absence of the corrosion potential difference [17,32–34]. In the cross-sectional view of the α -FeOOH and Fe₃O₄-covered specimens in Figure 10, obvious corrosion acceleration was observed. These results indicate that the α -FeOOH and Fe₃O₄ deposits can cause galvanic corrosion under stagnant conditions, while the Fe₂O₃ deposit did not cause a galvanic effect.

3.4. Surface Characterization

Figure 11 shows the XRD results for the iron oxide-covered and uncovered specimens in the test solution for 340 h at 40 °C. In the Fe₃O₄-covered specimen, Fe and a few Fe₃O₄ peaks were observed. Similarly, in the case of the Fe₂O₃-covered specimen, Fe, Fe₂O₃, and a few Fe₃O₄ peaks were observed. The Fe₃O₄ and Fe₂O₃ deposits did not influence the formation of a thick surface film on the steel substrate. Even though the Fe₃O₄ peaks were observed in the Fe₂O₃ case, the Fe₃O₄ peaks overlapped with the Fe₂O₃-peaks and the intensity was insignificant. Thus, Fe₃O₄ was formed under the Fe₂O₃-covered state but the formation and reaction activities were too small. However, in the cases of α -FeOOH-covered and bare specimens, Fe₃O₄ diffraction peaks were observed. These results indicate that Fe₃O₄ is the main surface film on the bare state in the test environment, and α -FeOOH

influences the formation of the Fe_3O_4 surface film on the steel substrate compared to the Fe_2O_3 and Fe_3O_4 cases.

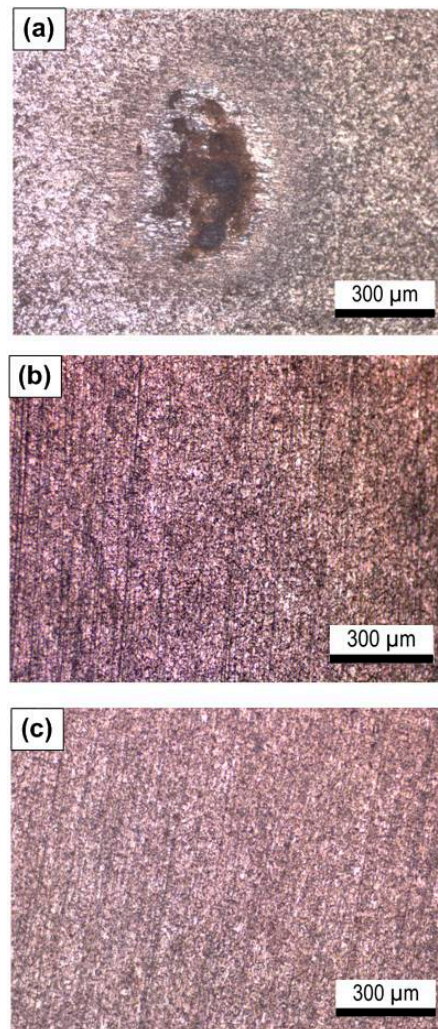


Figure 7. Optical microscope images of the specimens covered with (a) $\alpha\text{-FeOOH}$, (b) Fe_3O_4 and (c) Fe_2O_3 iron oxide deposits, after potentiostatic tests under $-650 \text{ mV}_{\text{SCE}}$ for 20 h in the simulated district heating water at $40 \text{ }^\circ\text{C}$.

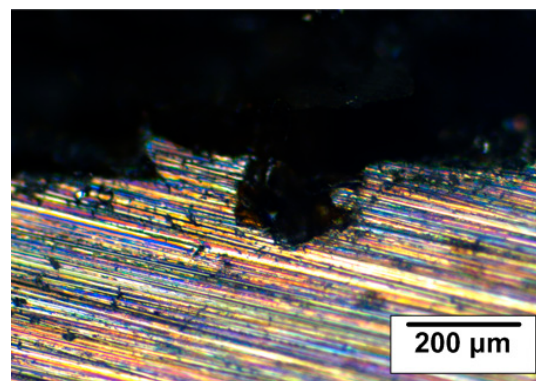


Figure 8. Cross-sectional image of the $\alpha\text{-FeOOH}$ -covered specimen after potentiostatic tests under $-650 \text{ mV}_{\text{SCE}}$ for 20 h in the simulated district heating water at $40 \text{ }^\circ\text{C}$.

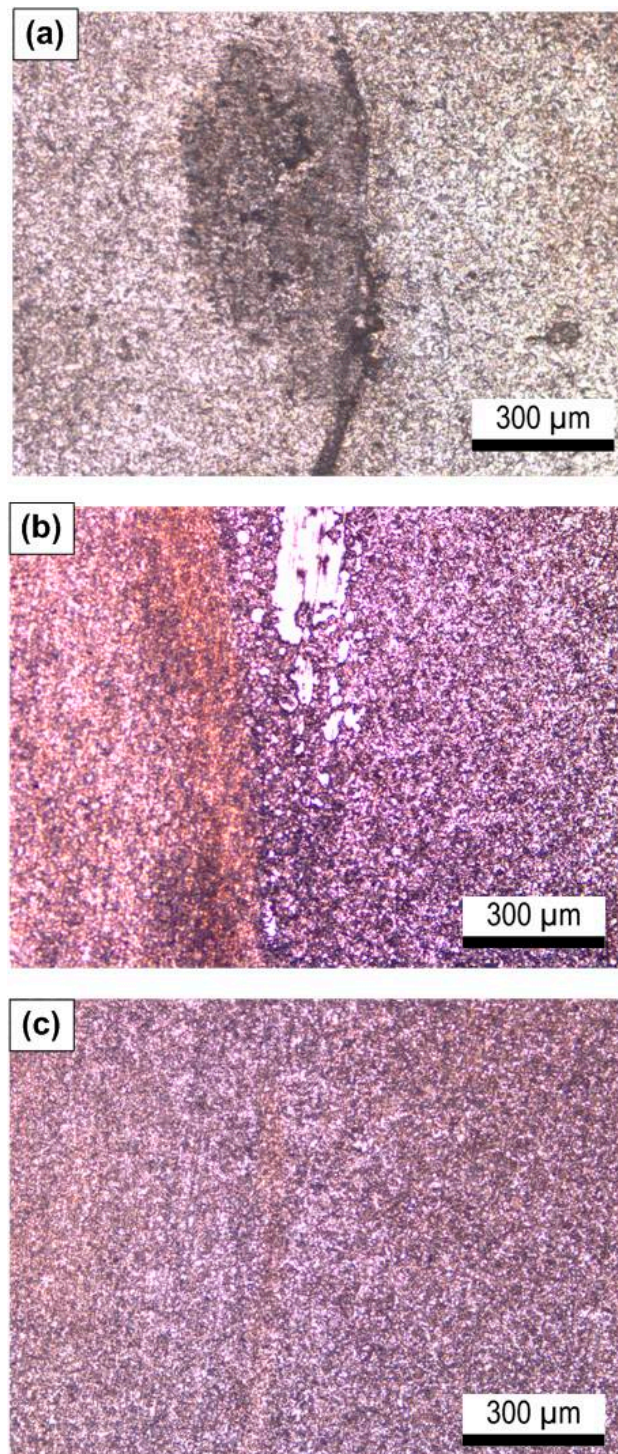


Figure 9. Optical microscope images of boundary covered (left side) and uncovered (right side) (a) α -FeOOH, (b) Fe₃O₄ and (c) Fe₂O₃ iron oxides deposit, after potentiostatic tests under $-650 \text{ mV}_{\text{SCE}}$ for 20 h in the simulated district heating water at 40 °C.

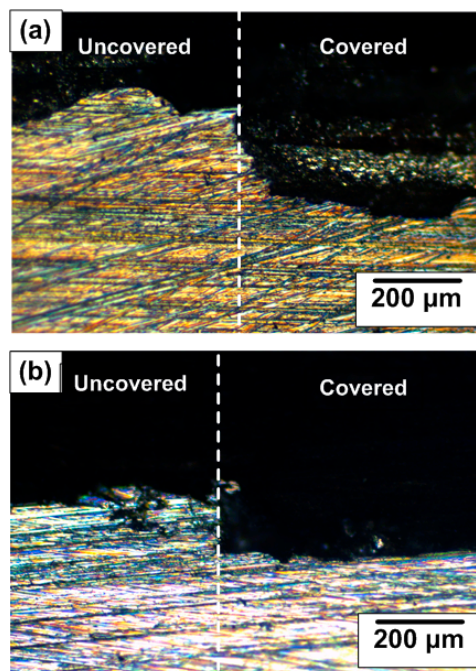


Figure 10. Cross-sectional images of the boundary of covered and uncovered (a) α -FeOOH, (b) Fe_3O_4 iron oxides deposit, after potentiostatic tests under $-650 \text{ mV}_{\text{SCE}}$ for 20 h in the simulated district heating water at 40°C .

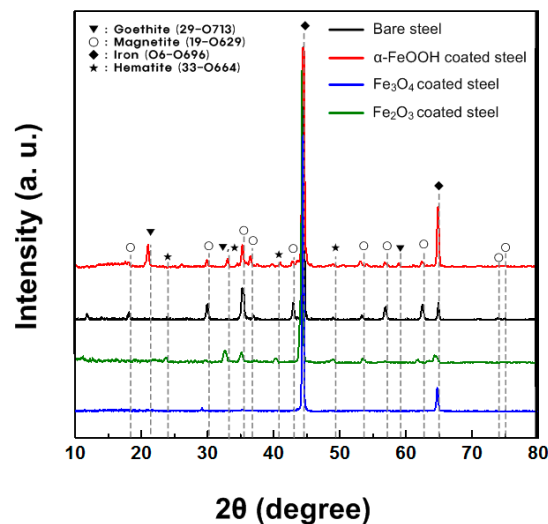


Figure 11. X-ray diffraction (XRD) spectra for the specimens covered with iron oxides and uncovered which were immersed in the simulated district heating water for 340 h at 40°C (∇ : goethite, α -FeOOH; \blacklozenge : iron, Fe; \circ : magnetite, Fe_3O_4 ; \star : hematite; Fe_2O_3).

3.5. Mott-Schottky Tests

It is well known that there is a relationship between the surface film properties related to the semiconducting behavior of a surface film and the corrosion behavior of materials [35,36]. These properties and behavior can be investigated by analyzing the curves of a Mott-Schottky plot. Thus, the surface film properties of a steel substrate under iron oxide deposits (α -FeOOH, Fe_3O_4 , Fe_2O_3) were investigated using a Mott-Schottky plot based on measurements of the electrode capacitance as a function of the electrode potential (E). It was assumed that the capacitance of the space-charge was much less than that of the Helmholtz layer, and thus the electrode capacitance was equal to C .

According to Mott-Schottky theory, the space-charge capacitance and n -type and p -type semi-conductors are given by Equations (5) and (6), respectively:

$$\frac{1}{C^2} = \frac{2}{\varepsilon\varepsilon_0eN_D} \left(E - E_{FB} - \frac{kT}{e} \right) \quad (5)$$

$$\frac{1}{C^2} = -\frac{2}{\varepsilon\varepsilon_0eN_A} \left(E - E_{FB} - \frac{kT}{e} \right) \quad (6)$$

where ε denotes the relative dielectric constant of the layer, ε_0 is the permittivity of a vacuum (8.8542×10^{-14} F/cm), e is the absolute value of the electron charge (1.6029×10^{-19} C), k is the Boltzmann constant (1.389×10^{-23} J/K), T is the absolute temperature, E_{FB} is the flat band potential that can be obtained from the extrapolation of $1/C^2$ to 0 V_{SCE} , and N_D and N_A are the donor and acceptor densities, respectively, which can be determined from the slope of the experimental $1/C^2$ versus applied potential [37–39].

Figure 12 shows the Mott-Schottky plots for the iron oxide-covered and uncovered specimens immersed in the test solution for 340 h at 40 °C. The slope of the Mott-Schottky diagram is negative, indicating p -type semiconducting behavior of the surface films in all conditions. In the iron oxides, the Fe_2O_3 and α -FeOOH indicate the n -type property whereas the Fe_3O_4 has p -type property [35]. It means that the Fe_3O_4 is mainly formed on the surface in all conditions. According to Equation (3), acceptor density (N_A) can be determined from the slope of the experimental $1/C^2$ versus E plots, i.e., more negative slope in Mott-Schottky plot suggests the decrease of acceptor density. Thus, the decrease of N_A was observed according to the following order: α -FeOOH < bare < Fe_2O_3 < Fe_3O_4 . The donor and acceptors in oxide layers are defects consisted of cation vacancies, anion vacancies and cation interstitials. Cation vacancies yielding p -type character acts as the doping element which prevents migration of cation from the metal surface and penetration of harmful anions such as Cl^- , F^- and SO_4^{2-} [36,40]. Thus, the semi-conductive properties of the oxide layer depend on the kind of oxide and the concentration of cation or anion vacancies. Although the increase of the N_A is related to the more disordered oxide layer and susceptible to corrosion in the passivity materials, this interpretation is not adequate in this study because the oxide layer was almost not formed on the Fe_2O_3 and Fe_3O_4 as shown in XRD results, and localized corrosion was only observed in the case of α -FeOOH-covered specimen. It is therefore the α -FeOOH on the surface and Fe_3O_4 formed beneath the α -FeOOH have an effect on the pitting corrosion.

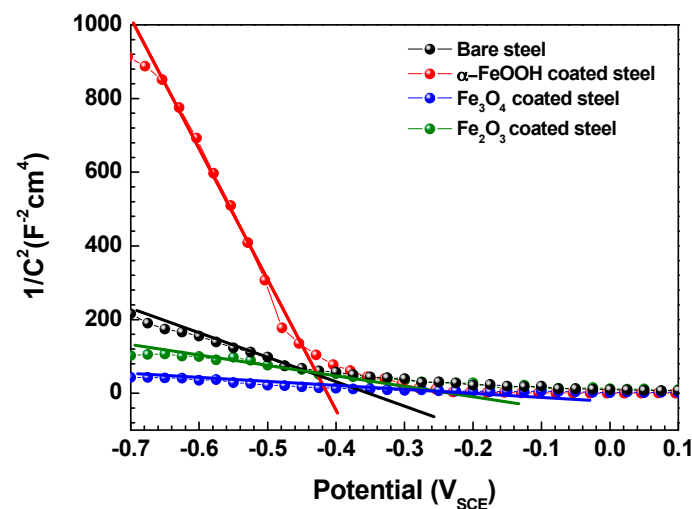


Figure 12. Mott-Schottky plots for iron oxides-covered and uncovered specimens immersed in the simulated district heating water for 340 h at 40 °C.

The thickness (W) of the space-charge layer, which is the surface film at a film formation potential, can be calculated by [41]:

$$W = \left(\frac{2\varepsilon\varepsilon_0}{eN_A} \right)^{\frac{1}{2}} \left(E_f - E_{FB} - \frac{kT}{e} \right)^{\frac{1}{2}} \quad (7)$$

In this equation, E_f is the film formation potential, and the other parameters have the same meanings as those in Equation (5). The film thickness (W) of space-charge layer is proportional to $1/C^2$ according to the following equation, obtained using Equations (6) and (7):

$$W = \varepsilon\varepsilon_0 \left(\frac{1}{C^2} \right)^{\frac{1}{2}} \quad (8)$$

Thus, W is increased in the following order: α -FeOOH > bare > Fe₂O₃ > Fe₃O₄. This indicates that the iron oxide deposits are not considered a surface film.

4. Discussion

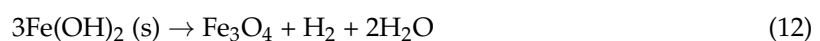
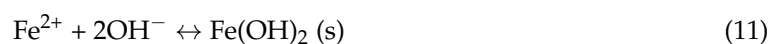
4.1. Surface Reaction under the Iron Oxide Deposits

The potentiodynamic polarization curves indicated a negative shift in the corrosion potential and an increase in the cathodic and anodic reactions on the iron oxide-covered specimens. The negative shift in the corrosion potential in the α -FeOOH and Fe₃O₄-covered specimens means that the increase in the anodic reaction area was due to the surface reaction from the Fe₃O₄ and α -FeOOH [42]. Additionally, the cathodic and anodic reactions for the α -FeOOH and Fe₃O₄-covered specimens increased. Therefore, the oxide deposit does not act as a surface barrier of the substrate, which is due to the porous properties of iron oxide particles [43].

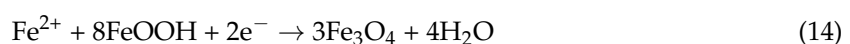
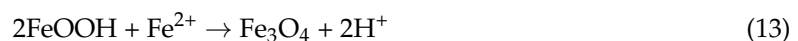
The following anodic and cathodic reactions occur on the steel substrate under the test solution conditions (de-aeration and pH 10). Equation (9) is the anodic dissolution and Equation (10) is the cathodic reaction in an alkaline solution under the de-aeration condition [44]:



Additionally, the Fe₃O₄ formation reactions occurred as shown in the XRD results according to the following Equations [45,46]:

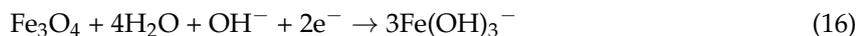
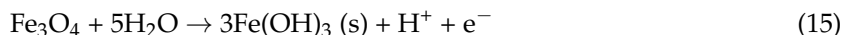


However, these surface film formation reactions are affected by the iron oxide deposits (α -FeOOH, Fe₂O₃, Fe₃O₄) on the substrate. Under the α -FeOOH and Fe₃O₄-covered specimens, the following cathodic and anodic reactions can occur. Under the α -FeOOH deposit, the following reactions occurred on the steel substrate [47–50]:



The reduction reaction of α -FeOOH occurred and due to these reduction reactions, the cathodic reaction was increased as shown by the polarization curve. In addition, with the increase in α -FeOOH reduction reactions, more Fe²⁺ ions were required to satisfy the equilibrium of Equations (13) and (14) such that the anodic dissolution of Equation (9) was increased simultaneously, as shown by the increase in the anodic reaction in the polarization curve. Based on these reactions, the formation of Fe₃O₄ can occur under the α -FeOOH deposit.

Under the Fe₃O₄ deposit, the following reactions can occur on the substrate [44,50,51]:



Equations (15) and (16) indicate the oxidation and reduction of Fe₃O₄ with water and hydroxide ions in the test solution, respectively. These oxidation and reduction reactions of Fe₃O₄ are indicated by the increase in anodic and cathodic reactions in the polarization curve. Additionally, the Fe₃O₄ formation reaction on the substrate was obstructed because the Fe₃O₄ deposit existed on the substrate, which restricts the formation of Fe₃O₄ as a surface film on the substrate.

Under the Fe₂O₃ deposit, the following reaction occurs on the substrate [51,52]:



Hematite, Fe₂O₃, is the final oxidation product among the iron oxides [53]. Thus, reduction reaction, Equation (17), occurs; this increases only cathodic reaction of the Fe₂O₃-covered specimen, as indicated in the polarization curve. The formation of Fe₃O₄ under the Fe₂O₃ deposit can be induced by Equation (18), but the reaction is limited due to the multiple reaction steps of Fe(OH)₃[−]. Thus, the formation of Fe₃O₄ under the Fe₂O₃ deposit is difficult.

The above reaction results were confirmed by Mott-Schottky and XRD analysis. In the Mott-Schottky results, the *p*-type semiconducting property and film thickness increased in the following order: α-FeOOH > bare > Fe₂O₃ > Fe₃O₄. Additionally, Fe₃O₄, which has *p*-type semiconducting properties [54], was primarily formed on the α-FeOOH-covered and bare specimens, as shown in the XRD analysis results. The results indicate that different reactions on the surface caused by iron oxide deposits affect the formation of Fe₃O₄ on the surface. In addition, the semiconducting property of the iron oxide deposits, which means α-FeOOH and Fe₂O₃ are *n*-type and Fe₃O₄ is *p*-type, was not observed in the Mott-Schottky results [36,55]. This implies that the iron oxide deposit on the specimen could not be analyzed by the Mott-Schottky measurement because the iron oxide deposits did not act as a surface film or barrier but rather as a reactant similar to a catalyst on the surface.

4.2. Mechanism of Different Corrosion Behavior under the Iron Oxide Deposits

In the potentiostatic tests, uniform corrosion behavior was indicated in all conditions, except the α-FeOOH-covered specimen. Pitting corrosion only occurred under the α-FeOOH-covered specimen. Uniform corrosion under the iron oxide deposits occurs due to the diffusion of external factors such as water and anions in the test solution, which were associated with porous properties of iron oxides that were revealed by the EIS and Mott-Schottky tests [56]. Under the α-FeOOH, pitting corrosion was observed, indicating that the cathode and anode areas were separated on the substrate.

Localized corrosion of steel can occur due to rust on the steel surface [18]. Two types of localized corrosion such as the UDC and the crevice corrosion were observed in this study. The rust on the steel and iron at the initial stage of corrosion is generally composed of Fe(OH)₃, α-FeOOH, and Fe₃O₄ from each transformation. The rust is visualized schematically in Figure 13. Fe(OH)₃ was transformed into α-FeOOH and then α-FeOOH was transformed into Fe₃O₄, as described by Equations (11) and (12). Based on these reactions, porous defects such as cracks and voids were developed in the rust layer, and the outside environment reaches the metal. The corrosion in these defects initiates a reaction, but the Fe²⁺ and OH[−] ions cannot react directly because the remaining α-FeOOH rust obstructs their direct reaction. Due to these separated reactions, FeCl₂ and NaOH are formed in the anode and cathode regions, respectively. Acidification occurs due to the FeCl₂ in the anode region when the anode dissolution is accelerated. This corrosion under the thick rust layer can be considered crevice corrosion [19]. Figure 14 shows the crevice corrosion process under the α-FeOOH rust layer. Localized

corrosion occurred under the α -FeOOH-covered specimen, even though the passive behavior was not observed on the polarization curve.

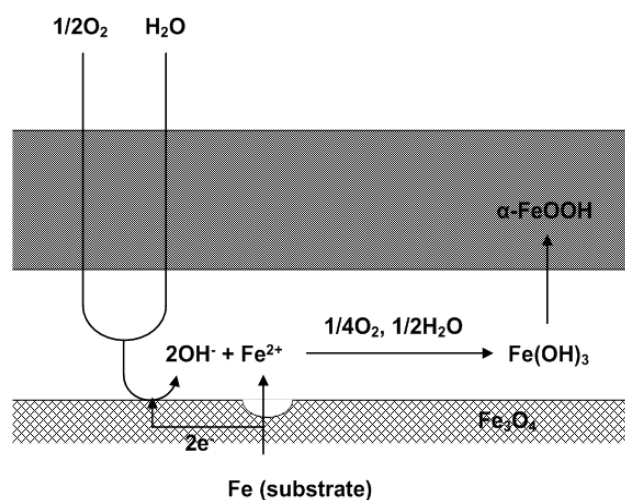


Figure 13. Schematic of the rust film formed on the steel at the initial stage of corrosion. Reproduced with permission from [18]. Copyright Elsevier, 2008.

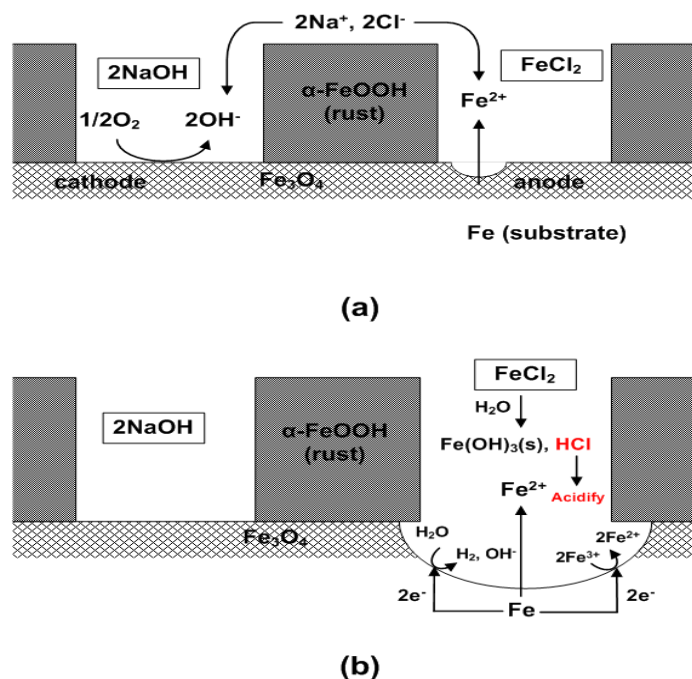


Figure 14. Mechanism of (a) crevice corrosion and (b) corrosion under the α -FeOOH rust.

5. Conclusions

(1) In the potentiodynamic polarization results, i_{CORR} increased in all deposit-covered specimens, which means that the corrosion reaction increased due to the deposit. The α -FeOOH and Fe_3O_4 -covered specimens demonstrate a negative shift in the corrosion potential and an increase in the number of anodic and cathodic reactions, and the Fe_2O_3 -covered specimen only increased the cathodic reaction.

(2) Pitting corrosion was only observed on the α -FeOOH-covered specimen, while uniform corrosion was observed on the others. This occurs due to a crevice corrosion phenomenon, which occurs via localized corrosion under the α -FeOOH rust layer on the steel substrate. Additionally,

the corrosion at the boundary between deposit-covered and uncovered pipe was observed on the α -FeOOH and Fe₃O₄ due to the galvanic effect.

(3) The Mott-Schottky and XRD analyses revealed that surface reactions differ according to the kind of iron oxide deposited, which influences the formation of surface film and the reaction rate of anode and cathode sites.

Based on this study, the iron oxides covered as a deposit on the steel substrate had a negative effect on the corrosion in district heating water. α -FeOOH can lead to localized corrosion, which causes failure in the early stage. Thus, stagnant condition prevention and floating matter filtration are important tasks for maintaining the pipeline. It would be helpful to purge with nitrogen to maintain a minimum flow rate rather than to fill the pipe with water during long downtimes.

Acknowledgments: This research was supported by the Global Ph.D. Fellowship Program through the National Research Foundation of Korea (NRF) funded by the Ministry of Education (2015H1A2A1033362).

Author Contributions: Jung-Gu Kim conceived and designed the experiments; Yong-Sang Kim performed the experiments; Jung-Gu Kim and Yong-Sang Kim analyzed the data; Jung-Gu Kim contributed reagents/materials/analysis tools; Yong-Sang Kim wrote the paper.

Conflicts of Interest: The authors declare no conflict of interest.

References

1. Wojdyga, K. An influence of weather conditions on heat demand in district heating systems. *Energy Build.* **2008**, *40*, 2009–2014. [[CrossRef](#)]
2. Ghafghazi, S.; Sowlati, T.; Sokhansanji, S.; Melin, S. A multi criteria approach to evaluate district heating system. *Appl. Energy* **2010**, *87*, 1134–1140. [[CrossRef](#)]
3. Harvey, L.D. *A Handbook on Low Energy Buildings and District Energy Systems: Fundamentals, Techniques and Examples*; Earthscan: London, UK, 2006.
4. *ECOHEATCOOL Workpackage 2: The European ColdMarket Final Report*; Euroheat & Power: Brussels, Belgium, 2016.
5. Cuddihy, J.; Kennedy, C.; Byer, P. Energy use in Canada: environmental impacts and opportunities in relationship to infrastructure systems. *Can. J. Civ. Eng.* **2005**, *32*, 1–15. [[CrossRef](#)]
6. Beckett, M.A.; Snoeyink, V.L.; Jim, K.; Sarin, P.; Kriven, W.M.; Lytle, D.A.; Clement, J.A. A pipe loop system for evaluating iron uptake in distribution systems. In Proceedings of the AWWA Water Quality Technology, San Diego, CA, USA, 12–13 November 1998.
7. Schock, M.R. Water quality and treatment. In *Internal Corrosion and Deposition Control*, 4th ed.; McGraw Hill: New York, NY, USA, 1990.
8. Rossum, J.R. Dead ends, red water, and scrap piles. *J. Am. Water Works Assoc.* **1987**, *79*, 113–115.
9. Kuppam, T. *Heat Exchanger Design Handbook*, 2nd ed.; CRC Press: New York, NY, USA, 2012.
10. Winters, M.A.; Stokes, P.S.N.; Zuniga, P.O.; Schlottenmier, D.J. Real-time performance monitoring of fouling and under-deposit corrosion in cooling water systems. *Corros. Sci.* **1993**, *35*, 1667–1675. [[CrossRef](#)]
11. Jeannin, M.; Calonnet, D.; Sabot, R.; Refait, P. Role of a clay sediment deposit on the corrosion of carbon steel in 0.5 mol L⁻¹ NaCl solutions. *Corros. Sci.* **2010**, *52*, 2026–2034. [[CrossRef](#)]
12. Pedersen, A.; Bilkova, K.; Gulbradsen, E.; Kvarekvål, J. CO₂ corrosion inhibitor performance in the presence of solids: Test method development. In Proceedings of the Corrosion Conference 2008, New Orleans, LA, USA, 16–20 March 2008; p. 632.
13. Tan, Y.J.; Fwu, Y.; Bhardwaj, K. Electrochemical evaluation of under-deposit corrosion and its inhibition using the wire beam electrode method. *Corros. Sci.* **2011**, *53*, 1254–1261. [[CrossRef](#)]
14. Lacroix, L.; Blanc, C.; Pébère, N.; Thompson, G.E.; Tribollet, B.; Vivier, V. Simulating the galvanic coupling between S-Al₂CuMg phase particles and the matrix of 2024 aerospace aluminium alloy. *Corros. Sci.* **2012**, *64*, 213–221. [[CrossRef](#)]
15. Dong, Z.H.; Shi, W.; Ruan, H.M.; Zhang, G.A. Heterogeneous corrosion of mild steel under SRB-biofilm characterized by electrochemical mapping technique. *Corros. Sci.* **2011**, *53*, 2978–2987. [[CrossRef](#)]
16. Turnbull, A.; Coleman, D.; Griffiths, A.J.; Francis, P.E.; Orkney, L. Effectiveness of corrosion inhibitor in retarding the rate of propagation of localized corrosion. *Corrosion* **2003**, *59*, 250–257. [[CrossRef](#)]

17. Zhang, G.A.; Yu, N.; Yang, L.Y.; Guo, X.P. Galvanic corrosion behavior of deposit-covered and uncovered. *Corros. Sci.* **2014**, *86*, 202–212. [[CrossRef](#)]
18. Tamura, H. The role of rusts in corrosion and corrosion protection of iron and steel. *Corros. Sci.* **2008**, *50*, 1872–1883. [[CrossRef](#)]
19. Bardal, E. *Corrosion and Protection*; Springer: London, UK, 2003.
20. Mansfeld, F. Tafel slopes and corrosion rates obtained in the pre-Tafel region of polarization curves. *Corros. Sci.* **2005**, *47*, 3178–3186. [[CrossRef](#)]
21. Stern, M.; Geary, A.L. Electrochemical polarization I. A theoretical analysis of the shape of polarization curves. *J. Electrochem. Soc.* **1957**, *104*, 56–63. [[CrossRef](#)]
22. Tromans, D.; Silva, J.C. Behavior of copper in acidic sulfate solution: Comparison with acidic chloride. *Corrosion* **1997**, *53*, 171–178. [[CrossRef](#)]
23. Huang, H.; Shaw, W.J.D. Electrochemical aspects of cold work effect on corrosion of mild steel in sour gas environments. *Corrosion* **1992**, *48*, 931–939. [[CrossRef](#)]
24. Kim, K.H.; Lee, S.H.; Nam, N.D.; Kim, J.G. Effect of cobalt on the corrosion resistance of low alloy steel in sulfuric acid solution. *Corros. Sci.* **2011**, *53*, 3576–3587. [[CrossRef](#)]
25. Lee, D.Y.; Kim, W.C.; Kim, J.G. Effect of nitrite concentration on the corrosion behaviour of carbon steel pipelines in synthetic tap water. *Corros. Sci.* **2012**, *64*, 105–114. [[CrossRef](#)]
26. Moretti, G.; Guidi, F.; Grion, G. Tryptamine as a green iron corrosion inhibitor in 0.5 M deaerated sulphuric acid. *Corros. Sci.* **2004**, *46*, 387–403. [[CrossRef](#)]
27. Mansfeld, F. Recording an analysis of AC impedance data for corrosion studies. *Corrosion* **1981**, *36*, 301–307. [[CrossRef](#)]
28. Tang, F.; Bao, Y.; Chen, Y.; Tang, Y.; Chen, G. Impact and corrosion resistances of duplex epoxy/enamel coated plates. *Constr. Build. Mater.* **2016**, *112*, 7–18. [[CrossRef](#)]
29. Mansfeld, F.; Kending, M.W.; Tsai, T. Recording and analysis of AC impedance data for corrosion studies II. Experimental approach and results. *Corrosion* **1982**, *38*, 570–580. [[CrossRef](#)]
30. Benedetti, A.V.; Sumodjo, P.T.A.; Nobe, K.; Cabot, P.L.; Proud, W.G. Electrochemical studies of copper, copper-aluminium and copper-aluminium-silver alloys: Impedance results in 0.5M NaCl. *Electrochim. Acta* **1995**, *40*, 2657–2668. [[CrossRef](#)]
31. Baraillon, C.; Brunet, S. Electrochemical impedance spectroscopy on oxide films formed on zircaloy-4 in high temperature water. *Electrochim. Acta* **1994**, *39*, 455–465. [[CrossRef](#)]
32. Barik, R.C.; Wharton, J.A.; Wood, R.J.K.; Stokes, K.R. Electro-mechanical interactions during erosion-corrosion. *Wear* **2009**, *267*, 1900–1908. [[CrossRef](#)]
33. Wilhelm, S.M. Galvanic corrosion in oil and gas production: Part 1-Laboratory studies. *Corrosion* **1992**, *48*, 691–703. [[CrossRef](#)]
34. Gao, G. Effect of salt deposition and temperature on polarization resistance of steel and the galvanic current of steel-aluminum couples during exposure to cyclic humidity. *Corrosion* **1999**, *55*, 432–437. [[CrossRef](#)]
35. Feng, Z.; Cheng, X.; Dong, C.; Xu, L.; Li, X. Passivity of 316L stainless steel in borate solution studied by Mott-Schottky analysis, atomic adsorption spectrometry and X-ray photoelectron spectroscopy. *Corros. Sci.* **2010**, *52*, 3646–3653. [[CrossRef](#)]
36. BenSalah, M.; Sabot, R.; Triki, E.; Dhoubi, L.; Refait, P.; Jeanin, M. Passivity of Sanicro28 (UNS N-08028) stainless steel in polluted phosphoric acid at different temperatures studied by electrochemical impedance spectroscopy and Mott-Schottky analysis. *Corros. Sci.* **2014**, *86*, 61–70. [[CrossRef](#)]
37. Zeng, Y.M.; Luo, J.L.; Norton, P.R. New interpretation of the effect of hydrogen on the ion distribution and structure of passive films on microalloyed steel. *J. Electrochem. Soc.* **2004**, *151*, B291–B298. [[CrossRef](#)]
38. Bott, A.W. Electrochemistry of semiconductors. *Curr. Sep.* **1998**, *17*, 87–91.
39. Montemor, M.F.; Ferreira, M.G.S.; Hakiki, N.E.; Belo, M.D.C. Chemical composition and electronic structure of the oxide films formed on 316L stainless steel and nickel based alloys in high temperature aqueous environments. *Corros. Sci.* **2000**, *42*, 1635–1650. [[CrossRef](#)]
40. Iken, H.; Basseguy, R.; Guenbour, A.; Bachir, A.B. Classic and local analysis of corrosion behaviour of graphite and stainless steels in polluted phosphoric acid. *Electrochim. Acta* **2007**, *52*, 2580–2587. [[CrossRef](#)]
41. Dan, T.; Shoji, T.; Lu, Z.; Sakaguchi, K.; Wnag, J.; Han, E.-H.; Ke, W. Effects of hydrogen on the anodic behavior of Alloy 690 at 60 °C. *Corros. Sci.* **2010**, *52*, 1228–1236. [[CrossRef](#)]

42. Staehle, R.W.; Royuela, J.J.; Raredon, T.L.; Serrate, E.; Morin, C.R.; Farrar, R.V. Effect of alloy composition on stress corrosion cracking of Fe-Cr-Ni base alloys. *Corrosion* **1970**, *26*, 451–486. [[CrossRef](#)]
43. Cornell, R.M.; Schwertmann, U. *The Iron Oxides: Structure, Properties, Reactions, Occurrences and Uses*, 2nd ed.; WILEY-VCH: Weinheim, Germany, 2003; pp. 95–109, 201–217.
44. Jones, D.A. *Principles and Prevention of Corrosion*, 2nd ed.; Prentice Hall: Upper Saddle River, NJ, USA, 1996; pp. 84–86.
45. Cabrera, L.; Gutierrez, S.; Menedez, N.; Morales, M.P.; Herrasti, P. Magnetite nanoparticles: Electrochemical synthesis and characterization. *Electrochim. Acta* **2008**, *53*, 3436–3441. [[CrossRef](#)]
46. Otake, T.; Wesolowski, D.J.; Anovitz, L.M.; Allard, L.F.; Ohmoto, H. Mechanism of iron oxide transformations in hydrothermal systems. *Geochim. Cosmochim. Acta* **2010**, *74*, 6141–6156. [[CrossRef](#)]
47. Evans, U.R. Mechanism of rusting. *Corros. Sci.* **1969**, *9*, 813–821. [[CrossRef](#)]
48. Evans, U.R.; Taylor, C.A.J. Mechanism of atmospheric rusting. *Corros. Sci.* **1972**, *12*, 227–246. [[CrossRef](#)]
49. Stratmann, M.; Bohnenkamp, K.; Engell, H.J. An electrochemical study of phase-transition in rust layers. *Corros. Sci.* **1983**, *23*, 969–985. [[CrossRef](#)]
50. Stratmann, M.; Hoffman, K. In situ Mößbauer spectroscopic study of reactions within rust layers. *Corros. Sci.* **1989**, *29*, 1329–1352. [[CrossRef](#)]
51. Fajaroh, F.; Setyawan, H.; Widiyastuti, W.; Winaradi, S. Synthesis of magnetite nanoparticles by surfactant-free electrochemical method in an aqueous system. *Adv. Powder Technol.* **2012**, *23*, 328–333. [[CrossRef](#)]
52. Allanore, A.; Lavelaine, H.; Valentin, G.; Birat, J.P.; Delcroix, P.; Lapique, F. Observation and modeling of the reduction of hematite particles to metal in alkaline solution by electrolysis. *Electrochim. Acta* **2010**, *55*, 4007–4013. [[CrossRef](#)]
53. Siebentritt, M.; Volovitch, P.; Ogle, K.; Lefèvre, G. Adsorption and electroreduction of hematite particles on steel in strong alkaline media. *Colloids Surf. A* **2014**, *440*, 197–201. [[CrossRef](#)]
54. Azumi, K.; Ohtsuka, T.; Sato, N. Mott-Schottky plot of the passive film formed on iron in neutral borate and phosphate solutions. *J. Electrochem. Soc.* **1987**, *134*, 1352–1357. [[CrossRef](#)]
55. Hakiki, N.E.; Boudin, S.; Rondot, B.; Belo, M.D.C. The electronic structure of passive films formed on stainless steels. *Corros. Sci.* **1995**, *37*, 1809–1822. [[CrossRef](#)]
56. Crolet, J.L. Mechanism of uniform corrosion under corrosion deposits. *J. Mater. Sci.* **1993**, *28*, 2589–2606. [[CrossRef](#)]



© 2017 by the authors. Licensee MDPI, Basel, Switzerland. This article is an open access article distributed under the terms and conditions of the Creative Commons Attribution (CC BY) license (<http://creativecommons.org/licenses/by/4.0/>).